

Dynamics of current sheet formation and reconnection in two-dimensional coronal loops

Z. W. Ma, C. S. Ng, Xiaogang Wang, and A. Bhattacharjee

Department of Physics and Astronomy, University of Iowa, Iowa City, Iowa 52242

(Received 11 January 1995; accepted 27 April 1995)

Current sheet formation and magnetic reconnection in a two-dimensional coronal loop with an X-type neutral line are simulated numerically using compressible, resistive magnetohydrodynamic equations. Numerical results in the linear and nonlinear regimes are shown to be in good agreement with a recent analytical theory [X. Wang and A. Bhattacharjee, *Astrophys. J.* **420**, 415 (1994)]. The topological constraint imposed by helicity-conserving reconnection is discussed. It is found numerically that helicity-conserving reconnection causes the initial X-point structure of the loop to change to Y points, with current sheets at the separatrices encompassing the Y points. Implications for observations are discussed. © 1995 American Institute of Physics.

I. INTRODUCTION

Two-dimensional (2-D) coronal loops with X-type neutral lines are of considerable interest from the standpoint of theory as well as observations. Such configurations are analytically and computationally tractable, and can represent with acceptable realism many observed features of coronal loops, reconstructed from X-ray images and magnetograms. In particular, it is widely believed that a study of such configurations can help elucidate the fundamental physical processes underlying a multitude of solar phenomena such as nanoflares, microflares, or x-ray bright points.

Several analytical and computational studies¹⁻⁹ of two-dimensional coronal loops with X-type neutral lines have been carried out, and have dealt with the issue of the existence of magnetostatic equilibria with current sheets. The general question that is addressed in these studies is the following: if we begin with an initial state that is a smooth solution of the magnetostatic equilibrium equations, is it possible, by means of smooth photospheric footpoint motions, to obtain neighboring equilibria with current sheets, i.e., singular current densities that result in jump discontinuities in the magnetic field? The existence of current sheets in the context of solar (and other astrophysical) plasmas has a crucial bearing on the coronal heating problem, as first pointed out by Parker,¹⁰ who has given a comprehensive discussion of this problem in a recent monograph.¹¹

The two-dimensional coronal loop with an X-type neutral line is a configuration in which there is no doubt regarding the tendency of the system to develop current sheets. This is because this system has well-defined separatrices, where the current density will tend to be singular for a large class of footpoint displacements. However, there has been some debate on the precise nature of the current singularities and the footpoint displacements that produce them. Finn and Lau⁸ have argued that some equilibrium current-sheet solutions discussed in the literature are characterized by footpoint displacements that have logarithmic singularities^{12,13} near the separatrix, and are therefore not admissible as a class of smooth, physical, footpoint displacements. To avoid these logarithmic singularities, Finn and Lau (as well as Vekstein and Priest⁹) have constructed scale-invariant equilib-

rium solutions that have smooth footpoint displacements and fractional power-law current singularities near the separatrix.

In all the analytical studies mentioned above, the focus is on the nature of the magnetostatic equilibrium solutions. The assumption is made implicitly that the coronal plasma will adjust to photospheric footpoint motion in order to maintain magnetostatic equilibrium, but no attempt is made to determine how rapidly in time the adjustment actually occurs. It should be emphasized that this is not merely an academic question. Observations of microflares and x-ray bright points in the solar corona exhibit a whole range of temporal dependencies from burstiness to relative quiescence, and the burden is on theory not only to provide a sequence of neighboring equilibria, but also to account for the time dependence of the growth and decay of an event.

Wang and Bhattacharjee¹⁴ (hereafter referred to as WB) have investigated analytically the time evolution of the magnetic and velocity fields in a two-dimensional coronal loop with an X-type neutral line using the incompressible resistive magnetohydrodynamic (MHD) equations. The initial state in WB is a vacuum state with a hyperbolic X point, shown schematically in Fig. 1. The coronal loop lies in the x - y plane, with the footpoints of the magnetic field lines intersecting the photosphere, which is taken to be a plane perpendicular to the plane of the paper. The separatrices $O_1O'_1$ and $O_2O'_2$ cross at O , which is the point of intersection of the X-type neutral line with the x - y plane. As this state is driven by smooth photospheric footpoint motion, it tends to develop current sheets at the separatrices. Using the ideal MHD equations, WB derive an exact solution for the linear regime and show that the transverse current sheet J_{\perp} (i.e., the current density perpendicular to \hat{z}) grows exponentially with time. Within a few characteristic Alfvén times, the effect of a small but finite resistivity slows down the rate of development of the current sheet. Subsequently, assuming that the footpoint motions at the boundary drive the system to a nonlinear regime, WB show that J_{\perp} saturates, and that the longitudinal current density J_z grows algebraically with time.

One of the principal goals of this paper is to test the analytical results of WB (and the generalizations thereof, given in this paper) by numerical simulation of the full re-

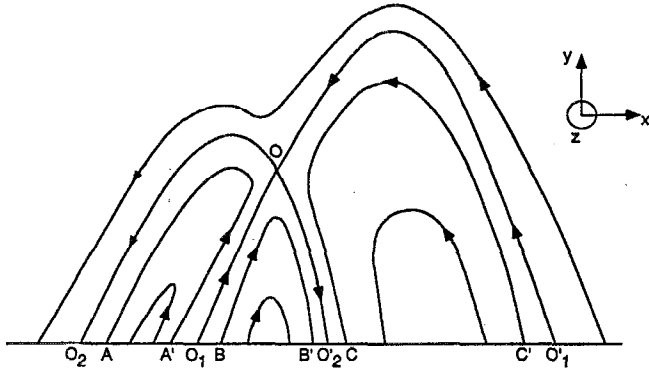


FIG. 1. Schematic picture of a two-dimensional coronal loop with an X-type neutral line that intersects the x - y plane of the loop at the point O.

sistive MHD equations, including the effect of plasma compressibility. The numerical results on the time development of the current sheet are found to be in good agreement with the analytical predictions, not only in the linear regime where the analytical solutions are exact, but also in the non-linear regime in which the analytical results are derived from some strong assumptions. We also demonstrate that when the reconnection dynamics forced by the footpoint motion is helicity conserving,^{15,16} the X-point structure in the initial state transforms to Y points.¹⁷

The following is a plan of this paper. In Sec. II, we generalize the analytical solutions of WB based on the incompressible MHD equations, including the effect of viscosity. In Sec. III, we discuss numerical results from the fully compressible code, and compare these results with the analytical predictions of WB. In Sec. IV, we present numerical results on the helicity conservation constraint. We conclude in Sec. V with a summary and a discussion of the implications of our results for observations.

II. SOME EXACT SOLUTIONS OF INCOMPRESSIBLE MHD

For configurations with translation symmetry along z , the magnetic field \mathbf{B} can be represented as

$$\mathbf{B} = \hat{\mathbf{z}} \times \nabla \psi + B_z \hat{\mathbf{z}}, \quad (1)$$

where ψ is a flux function. An incompressible flow field \mathbf{v} with the same symmetry can also be represented as

$$\mathbf{v} = \hat{\mathbf{z}} \times \nabla \phi + v_z \hat{\mathbf{z}}, \quad (2)$$

where ϕ is a streamfunction. The 2-D incompressible MHD equations for the four dependent variables, B_z , v_z , ψ , and ϕ can then be written (in cgs units) as

$$\frac{\partial B_z}{\partial t} + (\phi, B_z) = (\psi, v_z) + \frac{\eta c^2}{4\pi} \nabla^2 B_z, \quad (3)$$

$$\frac{\partial v_z}{\partial t} + (\phi, v_z) = \frac{1}{4\pi\rho} (\psi, B_z) + \frac{\nu}{\rho} \nabla^2 v_z, \quad (4)$$

$$\frac{\partial \psi}{\partial t} + (\phi, \psi) = \frac{\eta c^2}{4\pi} \nabla^2 \psi, \quad (5)$$

$$\frac{\partial \omega}{\partial t} + (\phi, \omega) = \frac{1}{c\rho} (\psi, J_z) + \frac{\nu}{\rho} \nabla^2 \omega, \quad (6)$$

where $J_z = (c/4\pi) \nabla^2 \psi$ is the longitudinal (or z component of the) current density, $\omega = \nabla^2 \phi$ is the z component of the vorticity, ρ is the (constant) density of the plasma, and $(f, g) = \hat{\mathbf{z}} \cdot \nabla f \times \nabla g$. The initial static equilibrium is taken to be a vacuum magnetic field described by

$$\psi_0 = b_0 x y / a, \quad (7)$$

where b_0 and a are constants, and the origin of the coordinate system is taken to coincide with point O in Fig. 1. In this initial state, $J_{z0} = 0$ and remains so for all times for continuous footpoint displacements in the z direction. As shown by WB and, more generally here, infinite-time current singularities develop in the transverse current density $\mathbf{J}_\perp = (\hat{\mathbf{x}} \partial B_z / \partial y - \hat{\mathbf{y}} \partial B_z / \partial x)$ in the ideal limit.

Equations (1)–(6) can be cast in dimensionless form by redefining $\mathbf{B}/b_0 \rightarrow \mathbf{B}$, $\mathbf{x}/a \rightarrow \mathbf{x}$, $t/\tau_A \rightarrow t$, $\psi/b_0 a \rightarrow \psi$, $\phi/\nu_A a \rightarrow \phi$, and $\omega \tau_A \rightarrow \omega$, where $\tau_A = a/\nu_A$ and $\nu_A = b_0/(4\pi\rho)^{1/2}$ is the Alfvén speed. The dimensionless equations are

$$\frac{\partial B_z}{\partial t} + (\phi, B_z) = (\psi, v_z) + \frac{1}{S} \nabla^2 B_z, \quad (8)$$

$$\frac{\partial v_z}{\partial t} + (\phi, v_z) = (\psi, B_z) + \frac{1}{R} \nabla^2 v_z, \quad (9)$$

$$\frac{\partial \psi}{\partial t} + (\phi, \psi) = \frac{1}{S} \nabla^2 \psi, \quad (10)$$

$$\frac{\partial \omega}{\partial t} + (\phi, \omega) = (\psi, J_z) + \frac{1}{R} \nabla^2 \omega, \quad (11)$$

where $S \equiv \tau_R/\tau_A$ is the Lundquist number, with $\tau_R \equiv 4\pi a^2/\eta c^2$, and $R \equiv \tau_r/\tau_A$ is the Reynolds number, with $\tau_r \equiv \rho a^2/\nu$.

It is clear by inspection of Eqs. (5) and (6) that the time evolution of ψ and ϕ is independent of B_z and v_z . This is a direct consequence of the assumption of incompressibility in two dimensions. Therefore, it is possible to solve for B_z and v_z with fixed ψ and ϕ , using suitable boundary conditions. In the ideal case, WB obtained a simple class of exact solutions of these equations. Here we give a general method for obtaining exact, time-dependent solutions of Eqs. (8) and (9), including the effects of dissipation in the special case $S=R$, with $\psi = \psi_0$ and $\phi = \phi_0 = 0$. (Note that the initial state in our study is a vacuum state that is qualitatively different from the stressed initial state considered in Refs. 18–20.)

Following WB, we define the Elsässer variables $f = B_z + v_z$, $g = B_z - v_z$. Equations (8) and (9) can then be combined to give

$$\frac{\partial f}{\partial t} = y \frac{\partial f}{\partial y} - x \frac{\partial f}{\partial x} + \frac{1}{S} \left(\frac{\partial^2 f}{\partial x^2} + \frac{\partial^2 f}{\partial y^2} \right) \quad (12)$$

and

$$\frac{\partial g}{\partial t} = -y \frac{\partial g}{\partial y} + x \frac{\partial g}{\partial x} + \frac{1}{S} \left(\frac{\partial^2 g}{\partial x^2} + \frac{\partial^2 g}{\partial y^2} \right), \quad (13)$$

which can be solved, subject to the initial conditions

$$f_0(x,y) \equiv f(x,y,t=0), \quad (14)$$

$$g_0(x,y) \equiv g(x,y,t=0). \quad (15)$$

Note that Eqs. (12) and (13) are linear. We now introduce the transformation

$$\xi = \lambda(t)y \equiv e^t y, \quad (16)$$

$$\zeta = x/\lambda(t), \quad (17)$$

$$T = \int_0^t \lambda^2(t') dt' = \left(\frac{1}{2}\right)(e^{2t} - 1), \quad (18)$$

whence Eq. (12) becomes

$$\frac{\partial F}{\partial T} = \frac{1}{S} \left(\frac{\partial^2 F}{\partial \xi^2} + \frac{1}{\lambda^4} \frac{\partial^2 F}{\partial \zeta^2} \right), \quad (19)$$

where $F(\xi, \zeta, T) = f(x, y, t)$. Setting $S = \infty$, we have the ideal solution $\partial F / \partial T = 0$, which implies that

$$F(\xi, \zeta, T) = F(\xi, \zeta, T=0) = f_0(\xi, \zeta) = f_0(ye^t, xe^{-t}). \quad (20)$$

Equation (19) can be solved exactly using a Green's function. The solution is

$$F(\xi, \zeta, T) = \frac{S\lambda^2}{4\pi T} \int_{-\infty}^{\infty} \int_{-\infty}^{\infty} d\xi' d\zeta' f_0(\xi', \zeta') \times \exp\left(-\frac{S}{4T} [(\xi - \xi')^2 + \lambda^4(\zeta - \zeta')^2]\right), \quad (21)$$

which gives

$$f(x, y, t) = \frac{S}{2\pi(1 - e^{-2t})} \int_{-\infty}^{\infty} \int_{-\infty}^{\infty} dx' dy' f_0(x', y') \times \exp\left(-\frac{S}{2(e^{2t} - 1)} [(ye^t - y')^2 + e^{4t}(xe^{-t} - x')^2]\right). \quad (22)$$

Equation (22) satisfies the initial condition (14). Equation (13), subject to the initial condition (15), can be solved in a similar manner. The solution is

$$g(x, y, t) = \frac{S}{2\pi(1 - e^{-2t})} \int_{-\infty}^{\infty} \int_{-\infty}^{\infty} dx' dy' g_0(x', y') \times \exp\left(-\frac{S}{2(e^{2t} - 1)} [(xe^t - x')^2 + e^{4t}(ye^{-t} - y')^2]\right). \quad (23)$$

From the functions f and g , we obtain

$$B_z(x, y, t) = \frac{1}{2}(f + g) \quad (24)$$

and

$$v_z(x, y, t) = \frac{1}{2}(f - g), \quad (25)$$

with the initial conditions

$$B_z(x, y, 0) = \frac{1}{2}(f_0 + g_0) \quad (26)$$

and

$$v_z(x, y, 0) = \frac{1}{2}(f_0 - g_0). \quad (27)$$

The exact solution obtained by WB from the linearized ideal equations is a special case of Eqs. (22) and (23). From the linearized resistive equations without viscosity, WB also obtained an asymptotic solution for a single Fourier component that holds in the restricted time domain $1 \ll t \ll S^{-1/3}$. In order to compare this asymptotic solution (in its domain of validity) with the exact solution obtained here, it will be necessary to complete the asymptotic solution by including the effect of viscosity and calculate the inverse Fourier-Laplace transform, after summing over all Fourier components. Though the methodology is well understood,^{21,22} there seems little point in pursuing it, now that we have the exact solutions.

Given initial conditions (14) and (15), we can easily carry out the integrals (22) and (23) (numerically, if necessary). In the Appendix, we discuss a special example for which one can solve Eqs. (12) and (13) analytically in closed form. Such exact, self-consistent solutions presented above allow us to settle some points of principle regarding the spatiotemporal structure of current sheets. These solutions are of interest because they exhibit current sheets with ψ frozen in the initial state (7) for all times, despite the presence of resistivity. [The resistive diffusion term on the right-hand side of Eq. (5) vanishes because $J_z = 0$, although $\eta \neq 0$.] However, these solutions cannot be regarded as generic because they are essentially linear for all times and the convective nonlinearities play no role in their evolution. A change in boundary conditions (such as the imposition of footpoint motions in the $x-y$ plane that direct flows toward the separatrix and tend to pile up flux there) or the inclusion of plasma compressibility, will make these special solutions irrelevant because nonlinear reconnection will change qualitatively the dynamics of the system. Indeed, it is not difficult to see that the exact solutions eventually evolve to a state in which the assumption of incompressibility, on which they are predicated, breaks down. This is because the time-dependent, incompressible solutions with steady ψ and ϕ must satisfy the condition

$$\nabla(p + B_z^2/2) = 0, \quad (28)$$

where p is the plasma pressure. As $t \rightarrow \infty$, $|\nabla B_z|$ becomes extremely large (infinity, in the ideal limit) at the separatrix, and it becomes impossible for the system to adjust to such large pressure gradients. Hence, even small departures from the incompressibility condition will lead to qualitative changes in the magnetic field geometry and flow pattern, and violate the condition of frozen-in ψ that holds for the exact, incompressible solutions. Magnetic reconnection will then intervene, changing qualitatively the nonlinear dynamics of the system.

III. COMPRESSIBLE DYNAMICS

The discussion at the end of Sec. II motivates us to include the effect of compressibility on the dynamics of the coronal loop. We have developed a computer code for this purpose, based on the following system of equations:

$$\frac{\partial \rho}{\partial t} = -\nabla \cdot (\rho \mathbf{v}), \quad (29)$$

$$\frac{\partial (\rho \mathbf{v})}{\partial t} = -\nabla \cdot \left[\rho \mathbf{v} \mathbf{v} + \left(p + \frac{B^2}{2} \right) \mathbf{I} - \mathbf{B} \mathbf{B} \right], \quad (30)$$

$$\frac{\partial \psi}{\partial t} = -\mathbf{v} \cdot \nabla \psi + \frac{1}{S} \nabla^2 \psi, \quad (31)$$

$$\frac{\partial B_z}{\partial t} = -\nabla \cdot (B_z \mathbf{v}) + \mathbf{B} \cdot \nabla v_z + \frac{1}{S} \nabla^2 B_z, \quad (32)$$

$$\frac{\partial p}{\partial t} = -\nabla \cdot (\rho \mathbf{v}) - (\gamma - 1) p \nabla \cdot \mathbf{v}. \quad (33)$$

Here \mathbf{I} is the unit dyadic, $\gamma (= \frac{5}{3})$ is the ratio of the specific heats of the plasma, the variables \mathbf{x} , \mathbf{v} , t , \mathbf{B} , and ψ are normalized to be dimensionless in the same manner as in Sec. II, and the pressure p is made dimensionless by scaling it with $b_0^2/4\pi$.

The initial force-free equilibrium containing an X-type neutral line is obtained by solving Laplace's equation $\nabla^2 \psi_0 = 0$ in the whole physical domain as a boundary-value problem. The flux function at the bottom boundary is chosen to be

$$\psi_0(x, y=0) = \begin{cases} \Psi_0 \sin[(2\pi a/L)(x_0 - x)], & x_1 < x < x_0, \\ \Psi_0 \sin[(2\pi a/L)(x_0 + x)], & -x_0 < x < -x_1, \\ 0, & \text{otherwise,} \end{cases} \quad (34)$$

where x_0 and x_1 are control parameters, chosen in this simulation to be equal to $0.7L/a$ and $0.2L/a$, respectively. The normalization constant Ψ_0 is chosen to make the dimensionless magnetic field \mathbf{B} unity on the boundary. The flux function is set to zero at the other three boundaries. The initial field configuration, which is determined by a numerical solution of Laplace's equation, is shown in Fig. 2. With the initial velocity and B_z set equal to zero, we have a static equilibrium.

Equations (29)–(33) are solved simultaneously using a Runge–Kutta finite-differencing scheme that has an accuracy of fourth order in time and second order in space. Exploiting the symmetry of the initial conditions, the numerical simulation is carried out in half of the physical domain in the x - y plane, with $x \in (0, 1)$ and $y \in (0, 2)$. To reduce numerical error and save computer time, we employ a nonuniform mesh. Nonuniform meshing enables us to increase resolution near the separatrix (where the current sheet develops) so that, with a 161×241 array, we can resolve 0.002 in x and 0.004 in y .

At the lateral mirror boundary $x=0$, dependent physical variables $G(x, y)$ are grouped as symmetric, i.e., $G(x, y) = G(-x, y)$, or antisymmetric, i.e., $G(x, y) = -G(-x, y)$. The fields ρ , p , v_y , ψ , and B_z are symmetric, whereas v_x and v_z are antisymmetric. The other lateral boundary $x=1$ as well as the upper boundary $y=2$ are treated as open, i.e., all variables except ψ obey the condition $\partial G/\partial t = 0$, and ψ obeys the condition $\partial \psi/\partial t = -\mathbf{v} \cdot \nabla \psi$. In order to reduce the amplitude of waves reflected from the boundary, a damping term is applied at the outermost grid points. A three-point differenc-

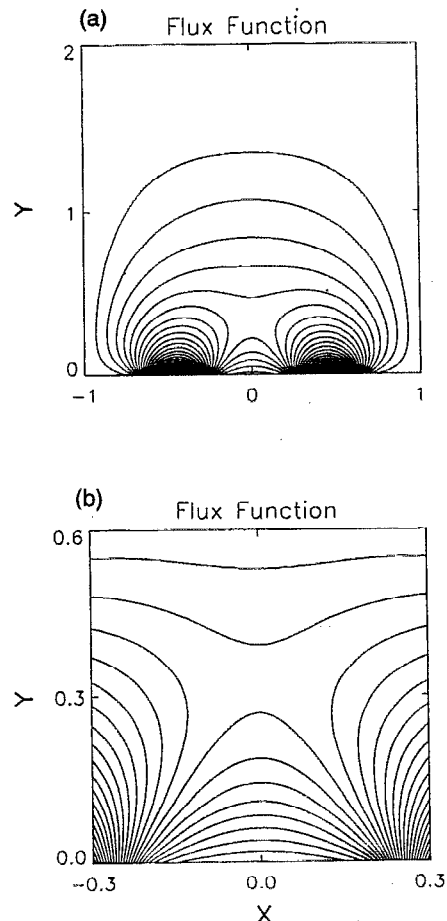


FIG. 2. Flux surfaces for a numerically generated vacuum-field solution of the 2-D loop. (b) is a magnified picture of the region around the X point in (a). This equilibrium solution is the initial condition for the compressible simulation.

ing method is used to calculate the first derivative at the boundary, ensuring second-order spatial accuracy.

The bottom boundary, assumed to simulate the photosphere, is treated as a material reservoir. All dependent variables on this boundary, except B_z and v_z , are held fixed at their initial values. Shearing motion of the footpoints along the z axis is prescribed according to the relation

$$v_z(x, y=0, t) = v_0 \tanh\left(\frac{t}{t_0}\right) \exp\left[-\left(\frac{x-x_0}{\Delta x}\right)^2\right], \quad (35)$$

where $x=x_0$ is the point at which the separatrix intersects the $y=0$ line. For the case studies discussed below, we have chosen $v_0=0.05$, $t_0=5$, and $\Delta x=0.05$. Since distances are normalized by a and time by τ_A , Eq. (35) describes smooth, coherent footpoint motions that build up to their maximum amplitude on a time scale that is nearly an order of magnitude larger than τ_A . The field B_z is obtained by direct numerical integration of Eq. (32), with one-sided differencing for derivatives with respect to y .

WB developed an analytical theory for the nonlinear regime, but they did not discuss the precise mechanisms by which the nonlinear regime may be realized. Footpoint motions in the x - y plane provide one way to realize the nonlin-

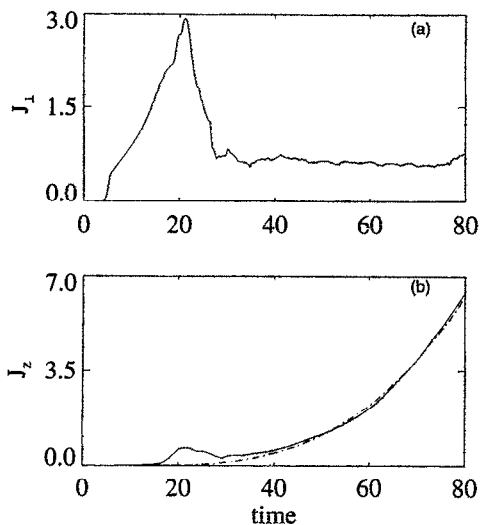


FIG. 3. Maximum amplitudes (a) $(J_{\perp})_{\max}$ and (b) $(J_z)_{\max}$ as a function of time from the compressible simulation with $S=2 \times 10^5$. The dashed line in (b) represents the analytically predicted t^3 behavior.

ear regime. Footpoint displacements in the z direction can also lead to the nonlinear regime, if plasma compressibility is invoked to couple ψ and ω with B_z and v_z . We pursue the second possibility here using our compressible code, and find that the results of the simulation on the time dependence of the current sheet development is in good accord with the analytical predictions of WB.

Figures 3(a) and 3(b) show the maximum amplitudes of $|J_{\perp}|_{\max}$ and $|J_z|_{\max}$, respectively, for a typical run with $S=2 \times 10^5$. In the linear and the early nonlinear phase (up to $t \approx 25$), the growth occurs primarily in J_{\perp} near the separatrix. In the linear phase, this growth is exponential in time, as

shown by WB, and confirmed by the numerical results. Subsequently, due to the dynamical coupling caused by finite plasma compressibility, the system enters a nonlinear phase in which J_{\perp} decays and saturates, while J_z grows algebraically in time to large values near the separatrix. WB predicted that this growth can be described by the relation $\psi \sim (S^{-1/2}t)^4$, which implies that

$$J_z \sim \eta t^3 - \eta^{-1/2} (t/\tau_{\text{SP}})^3, \quad (36)$$

where $\tau_{\text{SP}} \equiv (\tau_A \tau_R)^{1/2}$ is the characteristic Sweet–Parker time scale.²³ The dashed line in Fig. 3(b) is the analytically predicted t^3 behavior.

Figures 4(a) and 4(b) show the contour plots of J_z and ψ at $t=80$, respectively, for the run described in Fig. 3. Note the strong concentration of current density near the separatrix. The initial X-point structure of the separatrix has been altered to form Y points. This type of behavior has also been seen in the incompressible simulations of Biskamp²³ in a different geometry (with different boundary conditions). As explained in Sec. II, in the present geometry (Fig. 1) and with the boundary conditions (35), compressibility is crucial because it provides a mechanism for changing ψ by diffusion. Compressibility is known to play a similar role in numerical studies of magnetic arcade evolution (see, for instance, Biskamp and Welter²⁴ and other references therein).

IV. HELICITY-CONSERVING RECONNECTION AND Y POINTS

It has been suggested by Syrovatsky¹⁷ that current sheets will be formed along Y points in a 2-D, quasi-ideal, quasistatic plasma. (Interested readers will find a picture of Y points in the earlier work of Sweet,²⁵ who seems to have been aware of, but did not prove, the possibility of Y points

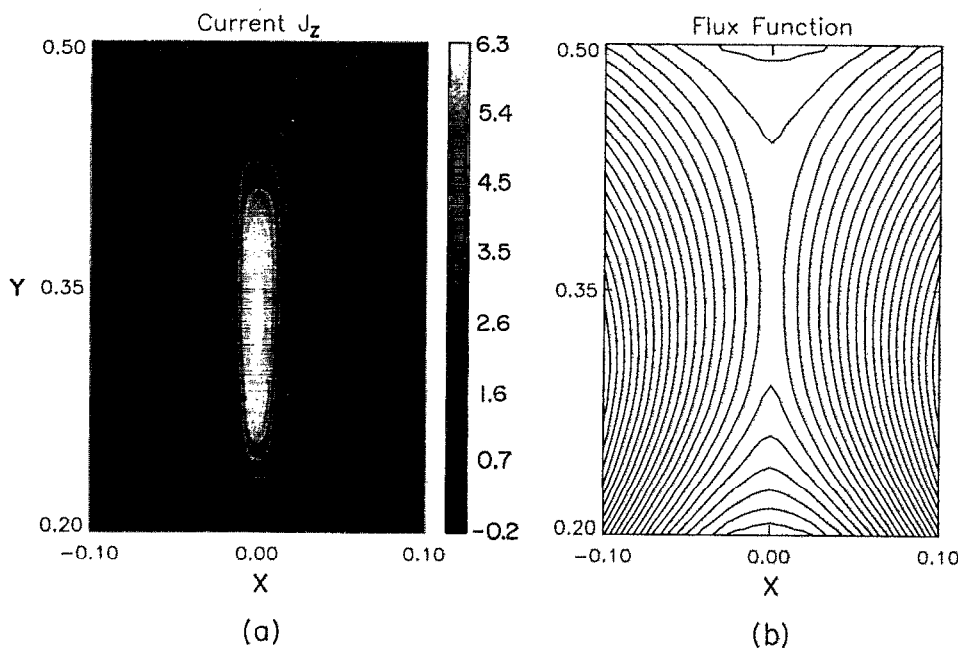


FIG. 4. Contour plots of (a) J_z and (b) ψ at $t=80$ for the compressible simulation with $S=2 \times 10^5$. Note the strong current sheet at the separatrix. The initial X-point structure, seen in Fig. 2, has changed to Y points.

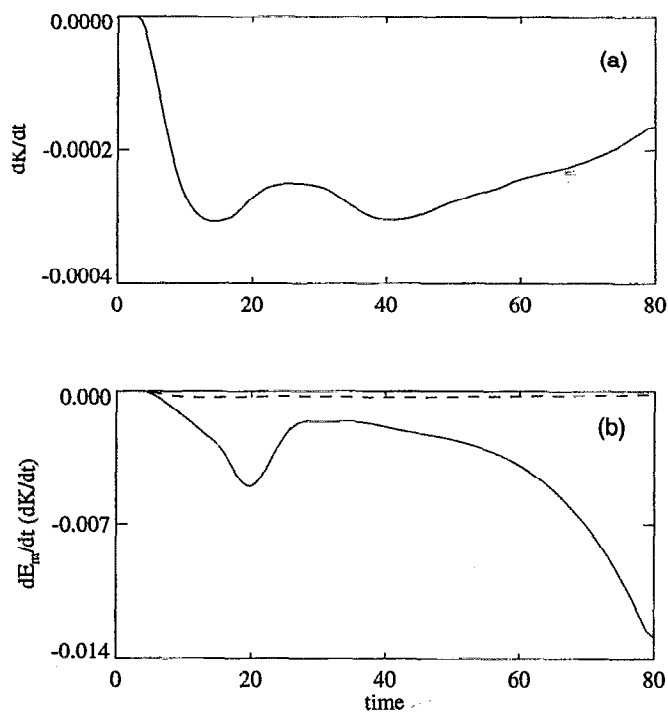


FIG. 5. Time rate of resistive decay of (a) magnetic helicity K and (b) magnetic energy E_m for the compressible simulation with $S=2 \times 10^5$. The rate of dissipation of energy is larger than that of helicity by nearly two orders of magnitude. The dashed line in (b) represents dK/dt .

in his steady-state reconnection model.) Further generalizations and refinements of Syrovatskii's 2-D results, derived using complex variable theory, have been given in Refs. 23 and 26–29. Although Syrovatskii's model is not fully self-consistent, its essential features have been confirmed by several self-consistent simulations in the regime of high Lundquist numbers.^{23,29–31}

Here we present numerical evidence that helicity-conserving reconnection leads to the formation of Y points in 2-D coronal loops. It should be emphasized that helicity is not an exact invariant in the presence of diffusion, and so helicity-conserving reconnection refers to dynamics that conserves helicity much better than energy. It is also important to note that here we are considering a stronger form of the helicity conservation constraint than used by Taylor.³² Taylor has discussed the self-organization of a strongly turbulent plasma in which it is not physically meaningful to speak of the topological identity of individual flux tubes. In a strongly turbulent system, Taylor has predicted that the total magnetic helicity is approximately conserved while the total magnetic energy decays rapidly. In contrast, what we have in mind is a much stronger form of the helicity conservation constraint, considered by Kadomtsev³³ and Bhattacharjee *et al.*,³⁴ who treat an unstable (but nonturbulent) plasma with well-defined magnetic surfaces nearly everywhere, in which magnetic helicity is conserved during “nonconstant- ψ ” reconnection. Since there are, in principle, an infinite number of flux tubes in a plasma with good surfaces, there are an infinite number of constraints, whereas the Taylor relaxation theory keeps only one global constraint.³⁴ Using the form of the helicity

conservation constraint developed in Refs. 33 and 34, and building on the mathematical framework developed by Rosenbluth *et al.*,³⁵ Waelbroeck¹⁵ has shown that Y points develop in the nonlinear stage of a kink-tearing instability. Bhattacharjee and Wang¹⁶ have adapted Waelbroeck's method to a “long-thin” coronal tube and shown that current sheets develop along the separatrix spanning Y points. [The “long-thin” approximation is motivated by the fact that coronal loops with very large aspect ratios ($\sim 10^2$) are not uncommon.³⁶ The advantage of the approximation is that it makes the problem essentially two dimensional. Furthermore, the equilibrium is topologically sufficiently simple that it is possible to carry through an analytical calculation involving the helicity conservation constraint. However, such a calculation cannot be applied to all coronal tubes, because the simple notion of a 2-D separatrix does not carry over to a three-dimensional tube of finite length.]

In the present context, the law of helicity conservation means that the integral,

$$K = \int \mathbf{A} \cdot \mathbf{B} \, dx \, dy, \quad (37)$$

is (approximately) conserved for reconnecting flux tubes. Here $dx \, dy$ is the infinitesimal element of area in a section of a flux tube, bounded by two neighboring surfaces. It is easy to show that this is equivalent to the conservation of $\int dl/B$ for reconnecting flux tubes. Though simple in principle, it is difficult in practice to calculate K analytically for the complicated loop configurations of the type considered in this paper. It is easier to calculate the rate of resistive decay of helicity (and energy), because the dominant effect of re-

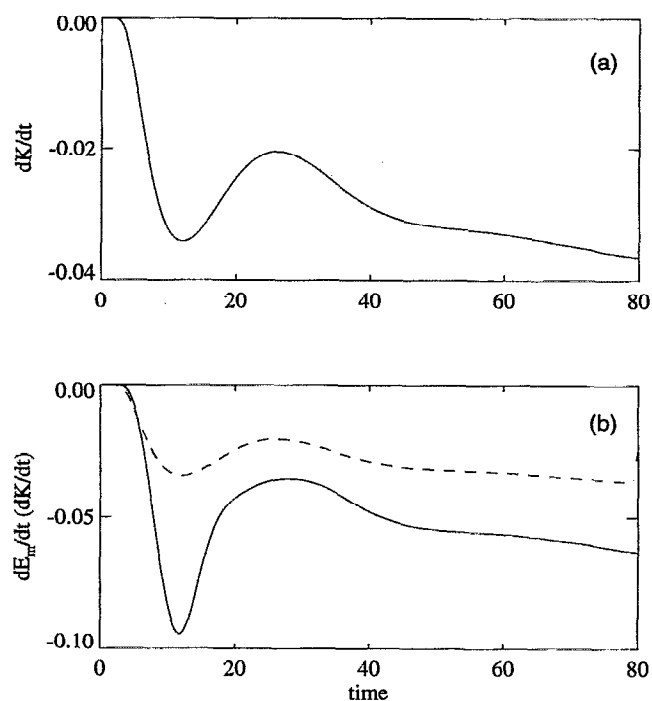


FIG. 6. Time rate of resistive decay of (a) magnetic helicity K and (b) magnetic energy E_m for the compressible simulation with $S=10^3$. The rate of dissipation of energy is comparable with that of helicity. The dashed line in (b) represents dK/dt .

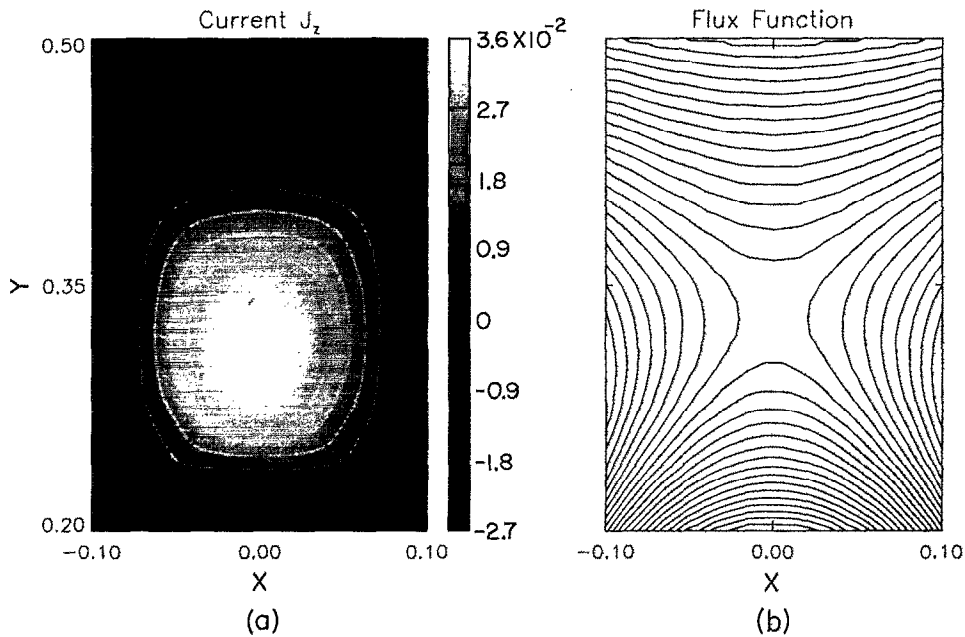


FIG. 7. Contour plots of (a) J_z and (b) ψ at $t=80$ for the compressible simulation with $S=10^3$. The amplitude of the current sheet is smaller, and it is less localized than it is in Fig. 4. The Y points are not well formed.

sistivity is localized near the separatrix where reconnection occurs. In Fig. 5, we show dK/dt and dE_m/dt (where $E_m \equiv \int dx dy B^2/2$) for the computer runs described in Figs. 3 and 4, with $S=2 \times 10^5$. The integrals are taken over a rectangular box that encompasses the reconnection layer. Though the magnetic helicity is not a constant [as indicated by the temporal variation in Fig. 5(a)], the change in helicity is approximately two orders of magnitude smaller than the change (loss) of energy. Hence, helicity can be regarded as approximately constant on the time scale magnetic energy

decays. The numerical evidence supports the basic theoretical claim¹⁴⁻¹⁶ that Y points are formed in helicity-conserving reconnection.

It is interesting to contrast the results of Fig. 5 with Fig. 6, which begins with the same initial condition, but uses a much lower value of $S (=10^3)$. In the latter case, the rates of resistive decay of helicity and energy are comparable, and helicity cannot be regarded as a good invariant while energy decays. Figure 7 shows the contour plots of ψ and J_z in this case, and it is obvious by inspection that the dynamics does not yield Y points. The current sheet J_z is also much weaker and spread out over a much broader diffusion layer. Figures 8(a) and 8(b) show the time evolution of J_{\perp} and J_z , respectively. The system evolves into the nonlinear phase very quickly, and the nonlinear growth of J_z is approximately linear in time (dashed curve), which is at variance with the analytical predictions and the numerical results given in Fig. 3. This underscores an issue that is central to discussions of current sheets and magnetic reconnection: low- S simulations ($\leq 10^3$) generally exhibit such large differences from high- S simulations ($\geq 10^5$) and analytical theories that it is difficult to extrapolate quantitative scalings obtained from low- S simulations to the high- S regimes that are believed to be observationally relevant for the solar corona.

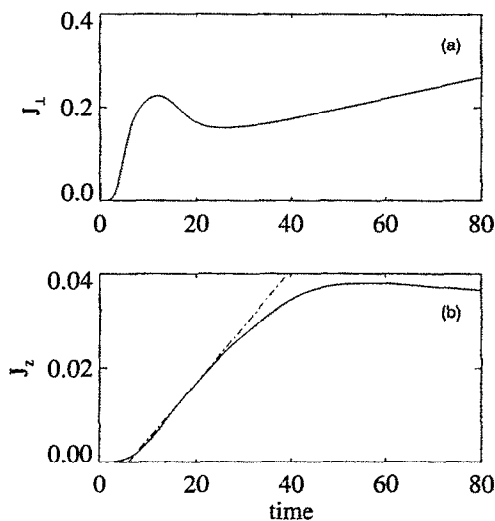


FIG. 8. Maximum amplitudes (a) $(J_{\perp})_{\max}$ and (b) $(J_z)_{\max}$ as a function of time from the compressible simulation with $S=10^3$. The dashed line in (b) is an approximate fit and shows $(J_{\perp})_{\max}$ increasing linearly with time.

V. SUMMARY AND DISCUSSIONS

The results of this paper, when combined with those obtained earlier by Wang and Bhattacharjee,¹⁴ provide a detailed description of the dynamics of current sheet formation in a two-dimensional coronal loop with an X-type neutral line. The emphasis in Ref. 14, as well as the present paper, is

on the precise time history of current sheets in such a loop beginning from a vacuum field, driven by smooth photospheric footpoint motion.

For compressible plasmas, we have presented numerical results on current sheet development in the linear and nonlinear stages of the dynamics. In the linear regime, on ideal time scales, current sheets tend to grow exponentially in J_{\perp} . This linear, ideal regime is followed by a short-lived linear, resistive regime before the system passes into the nonlinear regime on the characteristic Sweet–Parker time scale $(\tau_A \tau_R)^{1/2}$. In the early nonlinear regime, J_{\perp} saturates while J_z begins to grow. The growth in J_z is algebraic in time, proportional to t^3 , predicted by the analytical theory of WB and confirmed here by numerical solutions. It is found that the X-point structure of the separatrix in the initial state changes to Y points in helicity-conserving reconnection, as predicted by theory in the high- S regime.^{14–16}

It is worthwhile to reflect on the physical significance of these results, and what they imply for observations. For smooth initial conditions, all the current singularities we find are infinite-time singularities in the ideal limit. At least in the context of the present geometry, this should put to rest the question as to whether a true current singularity can be seen in ideal simulations by extrapolating to zero mesh size. As discussed in Ref. 14, the answer is no, because current singularities do not occur in finite time, even in the absence of dissipation. The current sheet keeps growing until it attains an amplitude large enough that the effect of diffusion has to be included as an essential part of the dynamics. It is interesting to note that the current sheet J_z , which actually owes its growth to the presence of diffusion and magnetic reconnection, ends up throttling the nonlinear reconnection dynamics to yield algebraic growth in time.

From the point of view of observations; there are several issues that need to be considered. It is clear that current sheets of the type considered here can produce significant coronal heating. Simple estimates, assuming that such sheets have a filling factor of the order unity, have been given in Ref. 14 and indicate that the heating produced can account for quiet loops and some, but not all, active loops. Direct observational tests of the validity of current sheet models, as discussed in considerable depth by Parker in his recent monograph,¹¹ involve several features that are beyond the scope of present-day observational techniques. The small spatial scales of current sheets are well below the spatial resolution of the state of the art instruments. One has to rely, therefore, on the integrated effect of numerous transient events as it affects a measurable quantity, but the interpretation of the latter is often subject to the uncertainties inherent in the various transport processes in the corona.³⁷ For example, assuming that the corona is made up of many hundred loops that are heated by nanoflares, Cargill³⁸ has developed a model to determine the dependence of the emission measure on temperature and established good correspondence with observations at temperatures in the range (10^5-10^6) K. But the modeling of the emission measure depends on parallel heat conduction, regarding which there are major uncertainties. In view of all this, as Cargill himself points out, one cannot regard agreement with emission measures in a re-

stricted temperature range, as sufficient evidence to rule exclusively in favor of current sheet models, but it is a minimum requirement that any heating mechanism should satisfy. For a comparative discussion of the various heating mechanisms and how they measure up against observations, the reader is referred to the recent review by Cargill,³⁹ who has also given an extensive bibliography.

Some of the more effective diagnostics for nonlinear reconnection theories are the observations on the temporal variation of hard x-ray emission (>10 keV). Hard x rays are a reliable signature of prompt electrons, and if one assumes that MHD activity causes the acceleration of electrons, then one can look at the temporal variation of the x-ray emission as a qualitative predictor of the time dependence of the electric field generated by reconnection. Such data is abundant from solar flares,⁴⁰ much less so for microflares,⁴¹ and non-existent for nanoflares. However, if we proceed on the tentative premise that reconnection phenomena of different degrees of virulence are responsible for the various types of flares, then one can hope to identify certain patterns in the time dependence of the x-ray emission, even if they correspond to events that differ vastly in the amount of energy liberated. [It is the amount of energy liberated that distinguishes a typical flare ($\sim 10^{33}$ ergs) from a typical microflare ($\sim 10^{27}$ ergs) and a typical nanoflare ($\sim 10^{24}$ ergs).] For instance, it is well known that in a typical flare, the time dependence of the hard x-ray emission exhibits an impulsive phase in which the emission exhibits a sudden transition in time from the slower growth phase. There is a similar trend in the data on microflares⁴⁰ that exhibit x-ray spikes, each of which one may assume is due to an individual reconnection event.¹¹ If we accept this sudden onset as a recurrent pattern, then the burden is on reconnection theories to account, not only for the rapidity of the impulsive phase, but the time development of the entire process, which includes the sudden transition to the impulsive phase. This is where nonlinear reconnection models, such as the one discussed in the present paper, run into difficulties, because in such models the reconnection dynamics passes from a linear exponential phase to an algebraic phase in time, and this is too qualitatively gradual to account for the sudden change in the time derivative of the emission profile, as the impulsive phase is triggered. It is possible that this discrepancy may be cured by considering a different class of boundary conditions at the photosphere or by going beyond the resistive MHD model to include other collisionless effects in a generalized Ohm's law. In the context of the analogous problem of sawtooth trigger in tokamaks, Wang and Bhattacharjee⁴² have recently shown that electron pressure gradient effects (in a generalized Ohm's law) can change the algebraic growth rates from nonlinear resistive MHD model to near-explosive growth. The exploration of this effect, as well as the dependencies on other types of footpoint motions on the boundary, is left to future work.

ACKNOWLEDGMENTS

This research is supported by the National Science Foundation Grant No. ATM 93-10157 and the Air Force Office of Scientific Research Grant No. F49620-93-1-0071.

APPENDIX: SOME EXACT INCOMPRESSIBLE SOLUTIONS

We consider some exact solutions of Eqs. (22) and (23). We take

$$B_z(x, y, t=0) = v_z(x, y, t=0) = B_0 \operatorname{erf}[-k(y+y_0)], \quad (\text{A1})$$

where erf denotes the error function, and B_0 , k , and y_0 are constants, with $k, y_0 > 0$. In particular, we choose $ky_0 \gg 1$, so that the initial perturbation of the separatrix is very small. The initial condition (A1) yields the exact, time-dependent solution,

$$B_z(x, y, t) = v_z(x, y, t) = B_0 \operatorname{erf}\left(-\frac{ke^t(y+y_0e^{-t})}{[1+(2k^2/S)(e^{2t}-1)]^{1/2}}\right). \quad (\text{A2})$$

The transverse current density is given by

$$\mathbf{J}_\perp = -\frac{2B_0}{\sqrt{\pi}} \frac{ke^t}{[1+(2k^2/S)(e^{2t}-1)]^{1/2}} \times \exp\left(-\frac{[ke^t(y+y_0e^{-t})]^2}{1+(2k^2/S)(e^{2t}-1)}\right) \hat{\mathbf{x}}. \quad (\text{A3})$$

For $t < (\frac{1}{2})\ln(S/2k^2)$, we obtain the ideal solution,

$$B_z(x, y, t) = v_z(x, y, t) = B_0 \operatorname{erf}[-ke^t(y+y_0e^{-t})], \quad (\text{A4})$$

with the transverse current density

$$\mathbf{J}_\perp = -\frac{2kB_0e^t}{\sqrt{\pi}} \exp[-k^2e^{2t}(y+y_0e^{-t})^2] \hat{\mathbf{x}}. \quad (\text{A5})$$

The right-hand side of Eq. (A5) tends to a δ function as $t \rightarrow \infty$. In other words, a current sheet is an infinite-time singularity of Eqs. (8)–(11) in the ideal limit.

For $t > (\frac{1}{2})\ln(S/2k^2)$, in the limit of large S , Eqs. (A3) and (A4) yield

$$B_z = B_0 \operatorname{erf}\left(-\sqrt{\frac{S}{2}}(y+y_0e^{-t})\right) \quad (\text{A6})$$

and

$$\mathbf{J}_\perp = -\sqrt{\frac{2S}{\pi}} B_0 \exp\left(-\frac{S}{2}(y+y_0e^{-t})^2\right) \hat{\mathbf{x}}, \quad (\text{A7})$$

respectively. As $t \rightarrow \infty$, Eqs. (A5) and (A6) describe a steady state in which there is a saturated current sheet at the separatrix, with an amplitude that increases as $S^{1/2}$ and a width that shrinks as $S^{-1/2}$.

For the general case $S \neq R$, although we have not found an exact, time-dependent solution, it can be shown that there exists a quasistationary solution to which the system may relax as $t \rightarrow \infty$. If the viscosity and resistivity are unequal, the equations for B_z and v_z are given, respectively, by

$$\frac{\partial B_z}{\partial t} = y \frac{\partial v_z}{\partial y} - x \frac{\partial v_z}{\partial x} + \frac{1}{S} \left(\frac{\partial^2 B_z}{\partial x^2} + \frac{\partial^2 B_z}{\partial y^2} \right) \quad (\text{A8})$$

and

$$\frac{\partial v_z}{\partial t} = y \frac{\partial B_z}{\partial y} - x \frac{\partial B_z}{\partial x} + \frac{1}{R} \left(\frac{\partial^2 v_z}{\partial x^2} + \frac{\partial^2 v_z}{\partial y^2} \right), \quad (\text{A9})$$

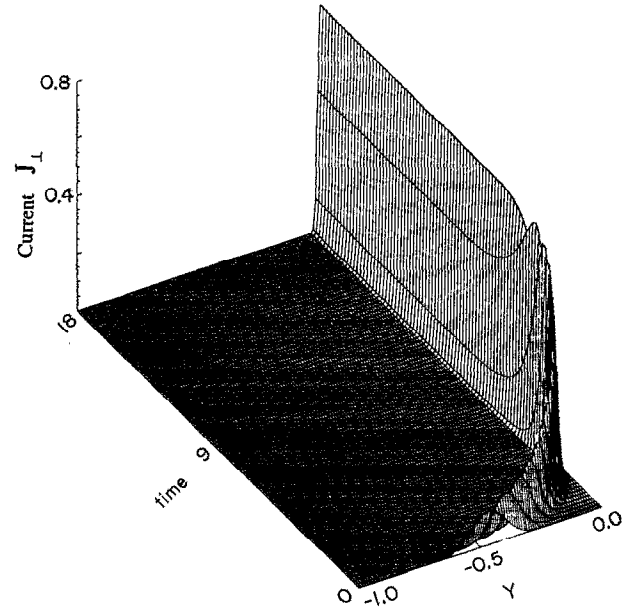


FIG. 9. The growth of a current sheet \mathbf{J}_\perp in an incompressible, resistive plasma without reconnection from the smooth initial condition (A1), with $S=R=10^4$. The current profile saturates as $t \rightarrow \infty$.

respectively. We investigate quasistationary solutions of Eqs. (A8) and (A9) in the limit $t \rightarrow \infty$. Setting $\partial B_z/\partial t = \partial v_z/\partial t = 0$, and defining $B' = B_z/k$, where k is a constant, we obtain

$$y \frac{\partial v_z}{\partial y} - x \frac{\partial v_z}{\partial x} + \frac{k}{S} \left(\frac{\partial^2 B'}{\partial x^2} + \frac{\partial^2 B'}{\partial y^2} \right) = 0 \quad (\text{A10})$$

and

$$y \frac{\partial B'}{\partial y} - x \frac{\partial B'}{\partial x} + \frac{1}{kR} \left(\frac{\partial^2 v_z}{\partial x^2} + \frac{\partial^2 v_z}{\partial y^2} \right) = 0. \quad (\text{A11})$$

In order to make Eqs. (A10) and (A11) symmetric, we choose $k = \sqrt{S/R}$. Defining new Elsässer variables, $f' = B' + v_z$ and $g' = B' - v_z$, we obtain the quasistationary solutions,

$$g' = 0 \quad (\text{A12})$$

and

$$f' = B_0 \left[1 + \operatorname{erf}\left(-\sqrt{\frac{S}{2k}} y\right) \right]. \quad (\text{A13})$$

Equations (A12) and (A13) yield

$$B_z = \frac{B_0}{2} \sqrt{\frac{S}{R}} \left\{ 1 + \operatorname{erf}\left[-\left(\frac{SR}{4}\right)^{1/4} y\right] \right\}, \quad (\text{A14})$$

which corresponds to a transverse current sheet with an amplitude directly proportional to $(S^3/R)^{1/4}$ and a width inversely proportional to $(SR)^{1/4}$.

We have developed a computer code that integrates Eqs. (8)–(11). This provides a check for the exact analytical solutions in the case $S=R$, and also determines the time development of the solutions in the cases $S \neq R$, which break the symmetry of Eqs. (12) and (13). In Fig. 9, we show the growth of the current sheet from the smooth initial state (A1)

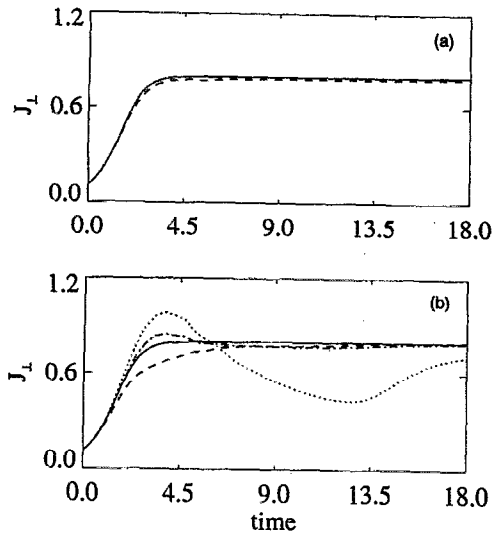


FIG. 10. (a) Comparison of the numerical (dashed line) and analytical (solid line) results for $(J_{\perp})_{\max}$ as a function of time, with $S=R=10^4$. (b) Numerical results for $(J_{\perp})_{\max}$ in three cases: $S=10^4$, $R=5 \times 10^3$ (---); $S=10^4$, $R=2 \times 10^4$ (-.-); and $S=10^4$, $R=\infty$ (···), compared with the exact analytical solution (solid line) for $S=R=10^4$, presented in Figs. 9 and (a).

to saturation for a case with $S=R$. In Fig. 10(a), we show that the numerical (dashed line) and analytical (solid line) results for the maximum transverse current density amplitude $(|J_{\perp}|_{\max})$ are in good agreement for the parameters of Fig. 9. In Fig. 10(b), we present the numerical solutions for $|J_{\perp}|_{\max}$ in three cases with $S \neq R$, and compare them with the analytical result of Fig. 10(a). As may be expected, the time development in Fig. 10(b) does deviate from the exact analytical prediction for $S=R$, and especially so for the case of zero viscosity. In the presence of viscosity, the mechanical oscillations are gradually damped, and the system tends to a quasistationary state.

- ¹J. J. Aly, in *Proceedings of the Workshop on Interstellar Magnetic Fields*, edited by R. Beck and R. Gräve (Springer-Verlag, Berlin, 1987), p. 240.
²H. K. Moffatt, in *Advances in Turbulence*, edited by G. Comte-Bellott and J. Mathieu (Springer-Verlag, Berlin, 1988), p. 228.
³B. C. Low and R. Wolfson, *Astrophys. J.* **324**, 579 (1988).
⁴T. H. Jensen, *Astrophys. J.* **343**, 507 (1989).
⁵J. T. Karpen, S. K. Antiochos, and C. R. Devore, *Astrophys. J.* **356**, L67 (1990).

- ⁶E. G. Zweibel and M. R. E. Proctor, in *Topological Fluid Mechanics*, edited by H. K. Moffatt (Cambridge University Press, Cambridge, 1990), p. 187.
⁷G. Vekstein, E. Priest, and T. Amari, *Astron. Astrophys.* **243**, 492 (1991).
⁸J. M. Finn and Y. T. Lau, *Phys. Fluids B* **3**, 2675 (1991).
⁹G. E. Vekstein and E. R. Priest, *Astrophys. J.* **384**, 333 (1992).
¹⁰E. N. Parker, *Astrophys. J.* **174**, 499 (1972).
¹¹E. N. Parker, *Spontaneous Current Sheets in Magnetic Fields* (Oxford University Press, New York, 1994).
¹²H. Grad, P. N. Hu, and D. C. Stevens, *Proc. Natl. Acad. Sci. USA* **72**, 3789 (1975).
¹³W. Zwingmann, K. Schindler, and J. Birn, *Sol. Phys.* **99**, 133 (1985).
¹⁴X. Wang and A. Bhattacharjee, *Astrophys. J.* **420**, 415 (1994).
¹⁵F. L. Waelbroeck, *Phys. Fluids B* **1**, 2372 (1989).
¹⁶A. Bhattacharjee and X. Wang, *Astrophys. J.* **372**, 321 (1991).
¹⁷S. I. Syrovatsky, *Sov. Phys. JETP* **33**, 933 (1971).
¹⁸I. J. Craig and A. N. McClymont, *Astrophys. J.* **393**, 385 (1992).
¹⁹A. B. Hassam, *Astrophys. J.* **399**, 159 (1992).
²⁰L. Ofman, P. J. Morrison, and R. S. Steinolfson, *Astrophys. J.* **417**, 748 (1993).
²¹T. S. Hahm and R. M. Kulsrud, *Phys. Fluids* **28**, 2412 (1985).
²²X. Wang and A. Bhattacharjee, *Phys. Fluids B* **4**, 1795 (1992).
²³D. Biskamp, *Phys. Fluids* **29**, 1520 (1986).
²⁴D. Biskamp and H. Welter, *Sol. Phys.* **120**, 49 (1989).
²⁵P. A. Sweet, *Electromagnetic Phenomena in Plasma Physics* (Cambridge University Press, Cambridge, 1958), p. 123; E. N. Parker, *J. Geophys. Res.* **62**, 507 (1957).
²⁶E. R. Priest and M. R. Raadu, *Sol. Phys.* **43**, 177 (1975).
²⁷Y. Q. Hu and B. C. Low, *Sol. Phys.* **81**, 107 (1982).
²⁸T. Amari and J. J. Aly, *Astron. Astrophys.* **227**, 628 (1990).
²⁹D. W. Longcope and H. R. Strauss, *Phys. Fluids B* **5**, 2858 (1993).
³⁰L. C. Lee and Z. F. Fu, *J. Geophys. Res.* **91**, 6807 (1986).
³¹E. R. Priest and T. G. Forbes, *J. Geophys. Res.* **97**, 16 757 (1992).
³²J. B. Taylor, *Phys. Rev. Lett.* **35**, 1139 (1974).
³³B. B. Kadomtsev, in *Plasma Physics and Controlled Fusion Research* (International Atomic Energy Agency, Vienna, 1977), Vol. I, p. 555.
³⁴A. Bhattacharjee, R. L. Dewar, and D. A. Monticello, *Phys. Rev. Lett.* **45**, 347 (1980).
³⁵M. N. Rosenbluth, R. Y. Dagazian, and P. H. Rutherford, *Phys. Fluids* **16**, 1894 (1973).
³⁶See, for instance, P. K. Browning, *Plasma Phys. Controlled Fusion* **33**, 539 (1991), and other references therein.
³⁷R. Rosner, W. H. Tucker, and G. S. Vaiana, *Astrophys. J.* **220**, 643 (1978).
³⁸P. J. Cargill, *Astrophys. J.* **422**, 381 (1994).
³⁹P. J. Cargill, in *Solar System Plasmas in Space and Time*, Geophysical Monograph 84, edited by J. L. Birch and J. H. Waite, Jr. (American Geophysical Union, Washington, DC, 1994), p. 21.
⁴⁰See, for instance, A. G. Emslie, *Sol. Phys.* **121**, 105 (1989).
⁴¹R. P. Lin, R. A. Schwartz, S. R. Kane, R. M. Pelling, and K. C. Hurley, *Astrophys. J.* **283**, 421 (1984).
⁴²X. Wang and A. Bhattacharjee, *Phys. Rev. Lett.* **70**, 1627 (1993).